Review of Scientific Instruments

Performance of JT-60SA divertor Thomson scattering diagnostics

Cite as: Rev. Sci. Instrum. **86**, 083511 (2015); https://doi.org/10.1063/1.4929514
Submitted: 20 May 2015 . Accepted: 13 August 2015 . Published Online: 28 August 2015

Shin Kajita, Takaki Hatae, Hiroshi Tojo, Akito Enokuchi, Takashi Hamano, Katsuhiro Shimizu, and Hisato Kawashima

Performance of JT-60SA divertor Thomson scattering diagnostics

Shin Kajita,[1,a)] Takaki Hatae,[2] Hiroshi Tojo,[2] Akito Enokuchi,[3] Takashi Hamano,[2] Katsuhiro Shimizu,[2] and Hisato Kawashima[2]
[1]*Nagoya University, Nagoya 464-8603, Japan*
[2]*Japan Atomic Energy Agency, Naka, Ibaraki 801-1, Japan*
[3]*Genesia Co., Mitaka, Tokyo 181-0013, Japan*

(Received 20 May 2015; accepted 13 August 2015; published online 28 August 2015)

For the satellite tokamak JT-60 Super Advanced (JT-60SA), a divertor Thomson scattering measurement system is planning to be installed. In this study, we improved the design of the collection optics based on the previous one, in which it was found that the solid angle of the collection optics became very small, mainly because of poor accessibility to the measurement region. By improvement, the solid angle was increased by up to approximately five times. To accurately assess the measurement performance, background noise was assessed using the plasma parameters in two typical discharges in JT-60SA calculated from the SONIC code. Moreover, the influence of the reflection of bremsstrahlung radiation by the wall is simulated by using a ray tracing simulation. The errors in the temperature and the density are assessed based on the simulation results for three typical field of views. © *2015 AIP Publishing LLC*. [http://dx.doi.org/10.1063/1.4929514]

I. INTRODUCTION

JT-60SA (JT-60 Super Advanced) is a satellite tokamak device in the broad approach, and it is planned at the moment to start operation from 2019.[1] One of the issues in future fusion devices is a control of particle and heat loads on materials. In JT-60SA, the steady state heat load can reach 10 MW/m^2 even under detached divertor conditions.[2] Since the ionization front is not so stable and it could be easily shifted to X-point MARFE (multifaceted asymmetric radiation from the edge),[3] which would degrade the energy confinement of the core plasma, it is inevitable to control the detached plasma. For that purpose, it is of importance to measure the plasma parameters in the divertor region and understand the behavior of detached plasmas including the ionization front.

One of the reliable measurement methods for the divertor plasmas is the laser Thomson scattering (LTS).[4] Other methods such as an electrostatic probe and spectroscopic methods have difficulty in measuring detached plasmas.[5–7] The LTS has an advantage that it can also be applied to detached plasmas, as demonstrated in DIII-D[4] and various linear devices.[8,9] In JT-60SA, the usage of LTS is under consideration,[1] and it is at the moment in the feasibility study phase. Although the temperature and density ranges and required accuracy were not defined in the research plan, the typical temperature and density ranges will be 0.5-200 eV and $>10^{19}$ m^{-3}, respectively, and the required accuracy will be 10%-20% in density and temperature.

Until now, a conceptual design[10] and an initial optical design have been conducted.[11] One of the serious issues to be considered is the limitation of the available space for collection optics. In a previous study, it was assessed that the measurement error in temperature would exceed 100% for the far field line of sight; it is necessary to improve the optical design to increase the collection solid angle. Moreover, for the assessment, there were assumptions in the plasma density, the temperature, and photon enhancement factor, which is mainly determined by reflection of bremsstrahlung radiation on the walls. Since the covered wavelength range is in near infrared wavelength, the line emissions are low and the major noise source for the LTS is from bremsstrahlung radiation. To accurately estimate the errors, it is necessary to consider the actual plasma distribution and the influence of the reflection of bremsstrahlung radiation.

In this study, we show an improved optical design and assess its performance in an accurate manner. To assess the influence, the profiles of the temperature, T_e, the density, n_e, and the effective charge, Z_{eff}, are calculated using the SONIC code,[12] and, moreover, the influence of the reflection of bremsstrahlung on walls is assessed using a ray tracing analysis. The errors in the temperature and density were assessed for two typical discharges.

II. COLLECTION OPTICS

A. Design of collection optics

Figure 1(a) shows a CAD (computer aided design) diagram of the divertor LTS measurement system. From the conceptual design, it was concluded that laser should be introduced from the lower port and the collection optics also should be equipped in the lower port plug. A commercially available Nd:YAG (neodymium-doped yttrium aluminum garnet) laser at 1064 nm with the pulse width of <10 ns is the candidate for the laser. The optics should be installed in a slender duct. In the previous design, the primary and secondary mirrors were installed in the top of the duct, which has only 40 mm in width. To increase the solid angle of the collection optics, we moved the collection optics to lower part, of which the available width is more than 100 mm, though the scattering angle should be

a)Electronic address: kajita.shin@nagoya-u.jp

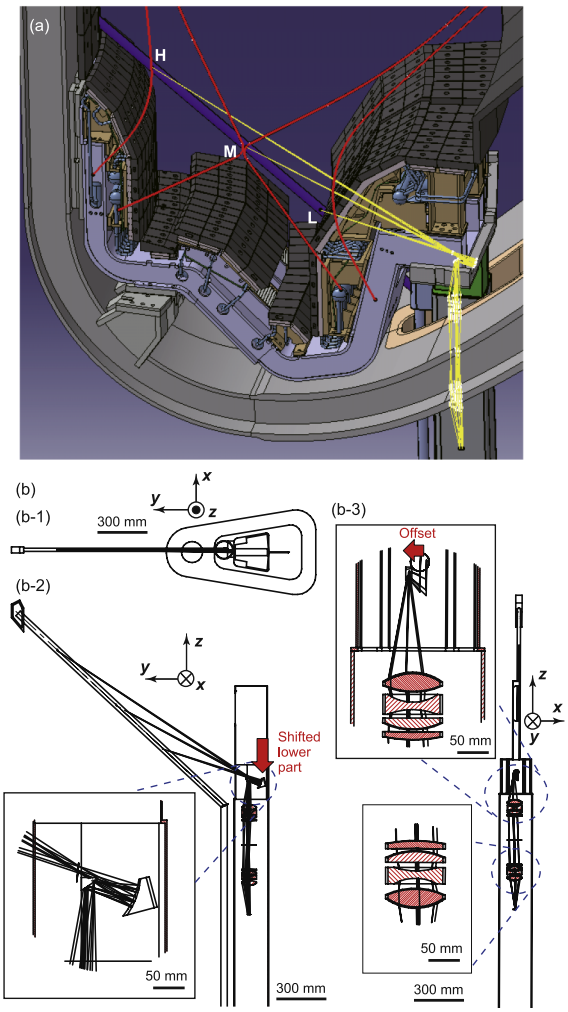

FIG. 1. (a) A CAD diagram of the divertor LTS measurement system and (b) schematics of the optics and typical rays seen from (b-1) top and (b-2) projected to a toroidal cross section, and (b-3) 90° rotated on the z-axis.

increased in the configuration. As shown in Fig. 1(a), typical three field of views (FOVs) are used for the assessment of the optical performance later. The measurement positions H, M, and L correspond to the high field side (HFS), middle, and low field side (LFS), respectively. The position M is close to the X-point.

In Fig. 1(b), schematics of the optics and typical rays seen from (b-1) top and (b-2) projected to a toroidal cross section, and (b-3) 90° rotated on the z-axis are shown. Three directions, x, y, and z are defined as shown in Fig. 1(b). Red arrows in Figs. 1(b-2) and 1(b-3) represent the major improvements in this study. In addition to shifting the mirrors to lower part, by shifting the primary mirror, which is the closest to the plasmas, in x direction, the interference of luminous flux with mechanical components including the secondary mirror is averted. Moreover, to increase the numerical aperture (NA) of the optics on the measurement (plasma) side, fiber collection optics, which was equipped in front of the optical fiber and had twice higher NA, was also used for the measurement side. Since we changed the lens system in the mirror side, further optimization was required for relay optical system. However, in this study, optimization of relay system was omitted and optical fiber was inserted in the middle of the port plug to focus on improving the optical performance. If the relay optical system is inevitable because of the deterioration of transmission of optical fiber by the influence of radiation, the relay system can be supplementary added without deterioration of optical performance. To design the optics, the commercially available optical design software CodeV (Synopsys, Inc.) was used. Optimization was performed for front end mirrors as fixing the lens system. The lens system was based on the one previously designed.

B. Optical performance

Figures 2(a) and 2(b) show the footprints of the rays on primary and secondary mirrors, respectively. The size of the primary and secondary mirrors are 32×50 and 10×24 mm^2, respectively. It is identified that the footprints are sufficiently smaller than the size of the mirrors. The shapes of the footprints were not round. This is because some rays to fibers are clipped by apertures of lens elements. This vignetting is caused by the pupil aberration mainly derived from the fact that only the mirror system was optimized using the lens system developed in the previous study for simplicity. It would be improved if the lens system was also optimized again.

Figures 2(c)-2(e) show the spot diagram at the measurement positions H, M, and L, respectively. In Figs. 2(c)-2(e),

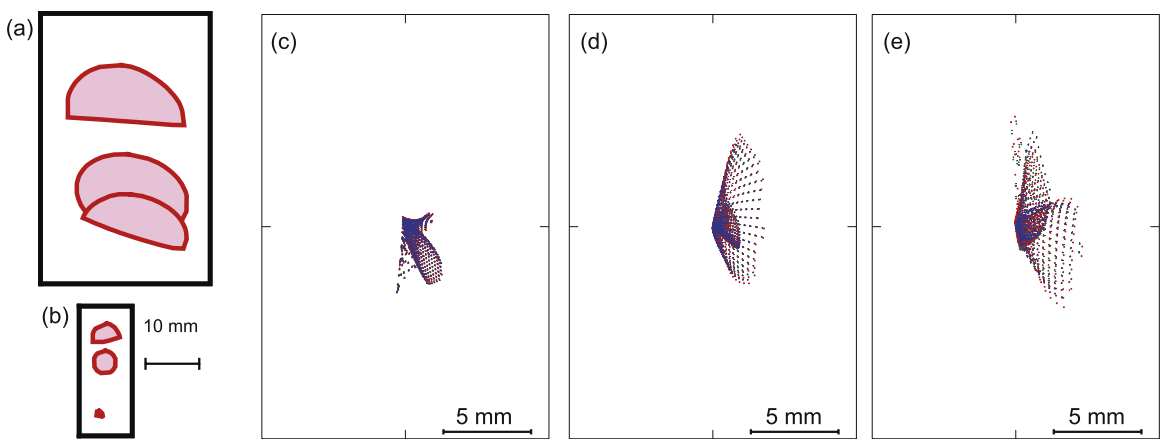

FIG. 2. Footprints of the rays on (a) primary and (b) secondary mirrors and the spot diagram at the measurement positions (c) H, (d) M, and (e) L.

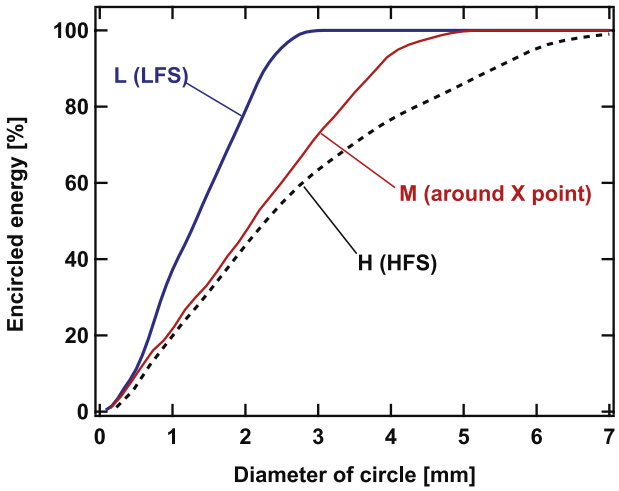

FIG. 3. The fraction of diffraction encircled energy as a function of the circle diameter at the measurement positions H, M, and L.

different colored dots show the spot diagrams at different wavelengths. The red and blue dots correspond to 1064 and 970 nm, respectively. It is seen that the distribution of the spots at the position L is broader than that at the position H. It is seen that the chromatic aberration is well compensated and much smaller than coma aberration, which is caused mainly by decentering the mirrors.

Figure 3 shows the fraction of diffraction encircled energy as a function of the circle diameter. The circle centers are placed at the chief ray position at the image. The fraction of the encircled energy increases gradually with the diameter and reaches ~80% when the diameter becomes ~2, 3.5, and 5 mm at the measurement positions of L, M, and H, respectively. The fraction of encircled energy almost reaches 100% when the diameter becomes 3, 5, and 7 mm at the measurement positions of L, M, and H, respectively. To obtain all the possible photon signals, it is necessary to expand the measurement region by 3–7 mm in addition to the laser diameter. The spatial resolution and the measurement region will be discussed later by considering the encircled energy profile in Fig. 3.

Table I shows the collection solid angle for L, M, and H measurement points. Previously, the solid angles for the three measurement points were 0.181, 0.049, and 0.009 msr, respectively. Thus, the present design improved the solid angle at L, M, and H positions by a factor of 2.3, 4.6, and 5.6, respectively. It is seen that the solid angle increased in the high field side in particular.

C. Spatial resolution

Discussion about the spatial resolution is provided here by considering the laser beam size, the scattering angle, and the encircled energy. The size of the laser beam has to be chosen by considering the multipulse laser induced damage threshold on the metallic mirrors, which has been measured previously.[13] It was concluded that the laser beam radius at the mirror should be 7.2 mm or more at 3.5 J and 10 mm or more at 7 J for the present configuration.[11] By focusing the laser beam around the X point, we can decrease the size of the laser beam at the measurement points H and L to approximately half of that at the laser transmission mirror. Assuming that the laser radius is 3.6 mm at the measurement points, the length of intersection between the laser and FOV along the laser beam becomes 40.8 mm at the position H and 15.4 mm at the position L. Moreover, considering the encircled energy of 80% fraction, the spatial resolution should be worsened by ~2-5 mm.

Figure 4 shows the spatial resolution as a function of the length of the scattering volume, ΔL, for the measurement positions H and L. The spatial resolution was defined here as the sum of the diameter of 80% fraction of the encircled energy and the length of the region in which 80% of the photons can be obtained from the total scattering volume. Previously, the length of the scattering volume was assumed to be 20 mm. However, considering the facts that spatial resolution cannot be less than ~40 and 15 mm at the positions H and L, respectively, and that the errors are marginal or serious especially in the position H as shown later, it would be better to increase ΔL from 20 mm. In this study, we assume ΔL = 30 mm at the position M and L and ΔL = 50 mm at the position H; the corresponding spatial resolution would be ~30 and 60 mm at the position L and H, respectively. At the position H, for example, though the resolution became approximately 1.5 times worse than the case of ΔL = 20 mm, the signal level increased significantly by a factor of three.

TABLE I. Solid angles for view cords L, M, and H.

View cord	Solid angle (msr)	Scattering angle (deg)
L (LFS)	0.409	155
M (Middle)	0.224	165
H (HFS)	0.050	170

III. MODELING

A. JT-60SA discharges

To assess the background bremsstrahlung and the LTS signal intensity accurately, the profiles of the plasma

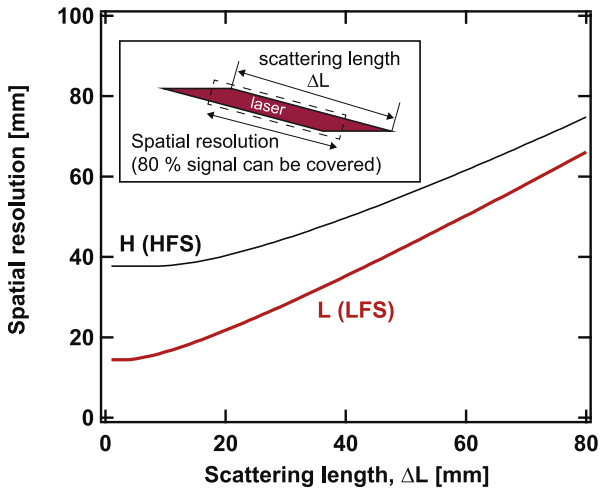

FIG. 4. Spatial resolution as a function of the length of the scattering volume for the measurement positions H and L. The spatial resolution was defined as the sum of the length in which 80% of the photons can be obtained and the diameter of 80% fraction of the encircled energy.

parameters are required. In this study, simulations were conducted using the SONIC code.[12] In the SONIC code, a Monte Carlo (MC) impurity code IMPMC is coupled self-consistently with a divertor code SOLDOR/NEUT2D and further coupled with a 3D plasma-surface interaction MC code EDDY. It makes it possible to investigate the details of impurity transport including erosion/redeposition processes on the divertor plates and influences to the core plasmas. Typical two discharges with the plasma current of 2.3 MA for the full current drive and 5.5 MA are chosen: they are called low density discharge and high density discharge, respectively, in this study. The density in the scrape off layer (SOL) should be low, say 1.6×10^{19} m^{-3} at the 2.3 MA operation. Consequently, the density is lower and the temperature is higher in the divertor region compared with the high density discharge. It was shown that the heat load can be acceptable even if the density is low by deuterium and argon gas puffs. On the other hand, the discharge at $I_p = 5.5$ MA is for achieving high plasma confinement performance.

In Fig. 5, calculated electron density and temperature profiles in the divertor region in the low density and high density discharges are shown. In the low density discharge, shown in Figs. 5(a) and 5(b), the density exceeded 10^{20} m^{-3} in the regions close to the strike points and X point. On the other hands, in the high density discharge, shown in Figs. 5(c) and 5(d), the density is significantly higher than that in the low density case, and the density is greater than 5×10^{19} m^{-3} in almost all the regions. Concerning the temperature, it is seen that the high density discharge has lower temperature than that in the low density discharge.

Figures 6(a) and 6(b) show profiles of the electron density and temperature along with the laser beam path, i.e. measurement positions, plotted as a function of the major radius, R. In the low density discharge, the density has a peak of $2-3 \times 10^{19}$ m^{-3} at around X-point ($R = 2.3$–2.4 m). The temperature also has a peak of 180 eV at $R \sim 2.25$. In the high density discharge, on the other hand, the density reaches 10^{20} m^{-3} in a wide region, and, moreover, it increases sharply and reaches 10^{21} m^{-3} around R of 2.3-2.4 m. In that region, the temperature is significantly low because the density is increased by the plasma flow toward X point from both high and low field sides. Because the magneto-hydrodynamic (MHD) equilibrium alters shot by shot, the laser beam went above the X-point in the low density discharge, while it went under the X-point in the high density discharge. In the high density discharge, the plasma region was only defined in $R < 2.0$ m. In the assessment, the density and temperature at $R = 2.0$ m were extended and used for the measurement point H ($R = 1.92$ m).

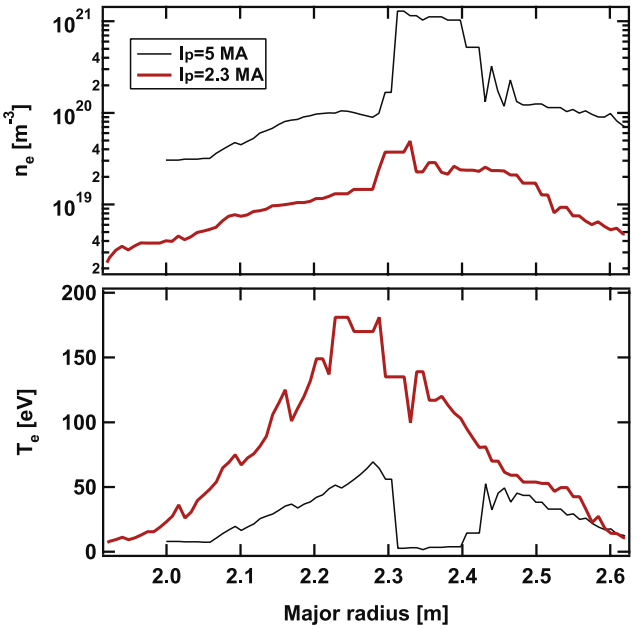

FIG. 6. The electron density and temperature profiles along with the laser beam path.

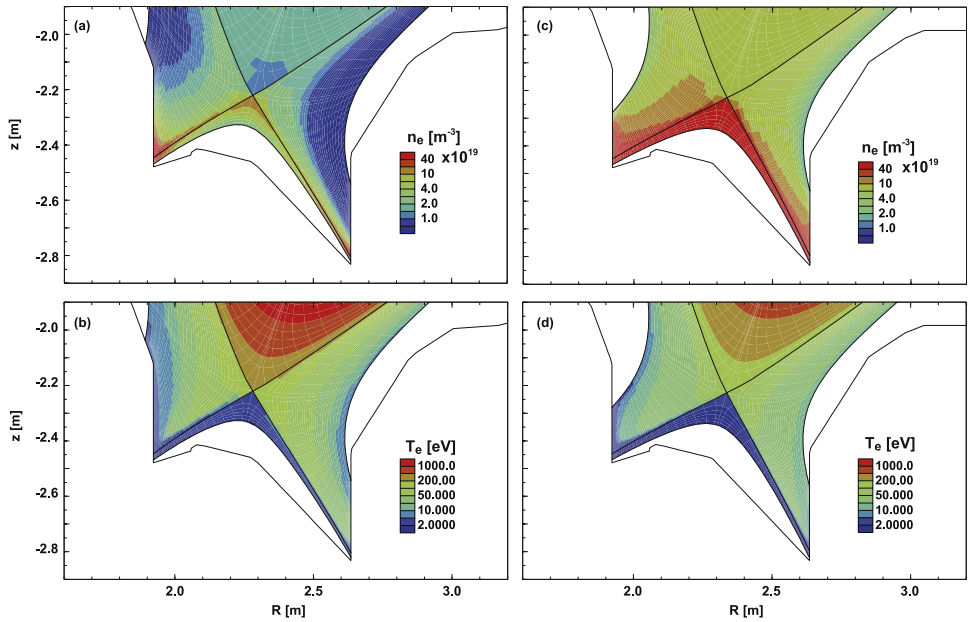

FIG. 5. Calculated electron density and temperature profiles using SONIC code. (a) and (b) are the density and temperature profiles in the low density discharge, and (c) and (d) are the density and temperature profiles in the high density discharge, respectively.

TABLE II. Segment points in wavelengths for the optical filters.

No.	Wavelength (nm)
5	978.7
4	1036.0
3	1053.0
2	1060.2
1	1064

B. Review the design of polychromator

After collecting the scattering light from the laser beam path by the collection optics, the light is transferred to spectrometers through optical fibers to resolve the spectrum. It is planned that multi-channel filter polychromators with avalanche photodiodes (APDs) for detector are used. The filters were optimized in the previous design.[10] However, since the scattering angle was changed, it was required to optimize the filter wavelength ranges again in the revised collection optics. The optimization of the filters was conducted using a simulated annealing method to minimize the sum of the averaged and maximum errors in the temperature in the range of 0.5-200 eV in the same manner as described in detail in Ref. 14. Table II shows the segment points in the wavelengths of the optimized optical filters used for the four channel polychromators. The band widths of the filters are in the range of 4-60 nm. The lower limit of the wavelength was ~980 nm similar to the previous study. Figure 7 shows the spectral density functions for HFS FOV at the temperature of 0.5, 10, and 200 eV and the transmission wavelength ranges of the band pass filters. Although the wavelength range is narrow at 0.5 eV, measurement can be properly conducted with using narrow band path filter such as 4 nm or less. The wavelength shifts of the segment points from the previous design were in the range of 1-4 nm. The optimized filters are used for the calculation later.

C. Modeling of light reflection

Influence of the reflection of photons in the vacuum vessel was investigated using a ray tracing simulation software

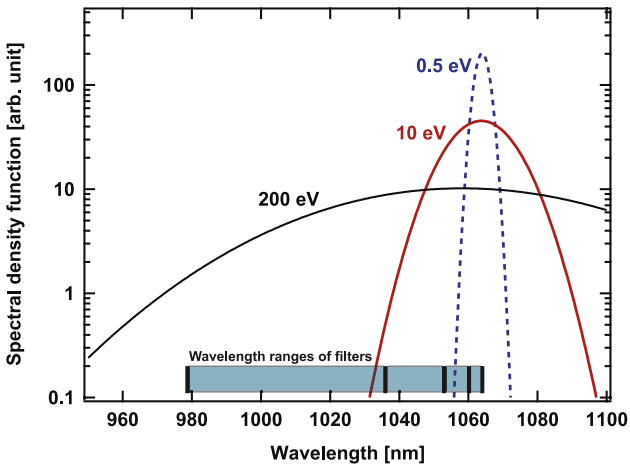

FIG. 7. Spectral density functions for HFS FOV at 0.5, 10, and 200 eV. The wavelength ranges of filters used for the noise assessment are also shown.

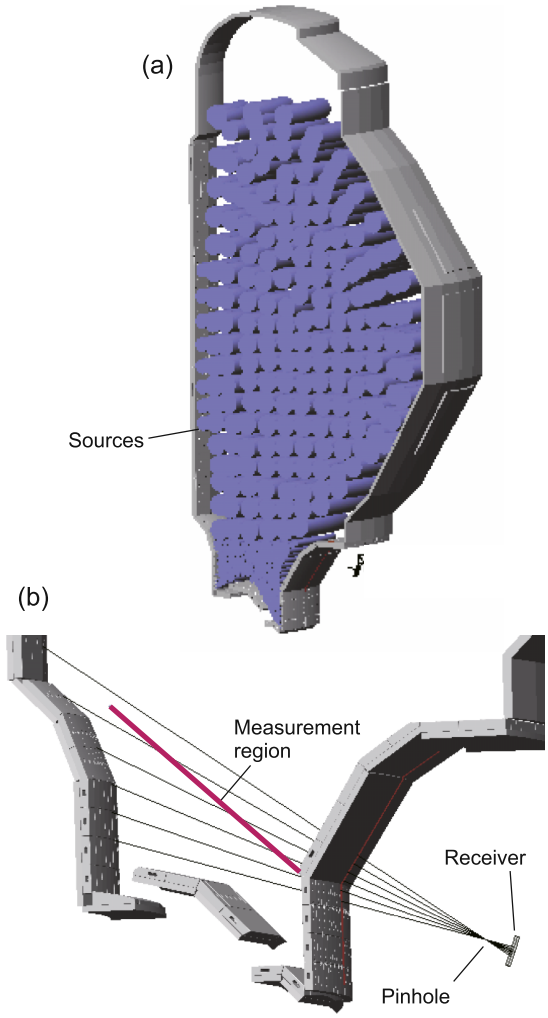

FIG. 8. Schematics of the model used for the simulation.

LightTools. Components of a 20° toroidal sector was installed in LightTools and used for the simulation, as shown in Fig. 8(a). In Fig. 8(a), blue colored toroidally shaped tubes show the sources of radiation. Because only the toroidally uniform sources are used in this study, the 20° toroidal sector model can be properly used effectively with shorter calculation time and less necessary memory size. The diameters of the sources were set to be 60 mm in the divertor region and 200 mm in the core and SOL regions. The bremsstrahlung power per wavelength was calculated using the calculated n_e, T_e, and Z_{eff} from the following equation:[15]

$$\epsilon_\lambda = \frac{P_{\mathrm{br}}(\lambda)}{\Delta\lambda} = \frac{1.89\times10^{-35} n_e^2 Z_{\mathrm{eff}}}{T_e^{1/2}\lambda^2} g_{\mathrm{eff}} \exp\left(-\frac{1240}{T_e\lambda}\right), \quad (1)$$

where λ is the wavelength in nm and g_{eff} is the Gaunt factor. The number of cells in the SONIC simulation was approximately 6000; to reduce the calculation time, the cells were added up and the number of the source was reduced to ~200 in the core and SOL regions and ~160 in the divertor region. The radiation from each cell is installed in the toroidal shaped sources.

A pinhole configuration without actual optical elements was used for the assessment, similar to the models used in previous studies on the ITER spectroscopy.[16] To accurately

assess the radiation profile in the pinhole configuration, a backward ray tracing is used for the analysis. In Fig. 8(b), a detailed schematic in the divertor region and rays from the receiver are shown. A slit with the width of 30 mm is made on the divertor cassette, and a receiver is positioned at the primary mirror position. In the backward ray tracing, rays are traced from the receiver to the measurement region through a small pinhole, which is much smaller than the distance between the pinhole and the receiver to obtain necessary spatial resolution on the receiver. The photon radiance in ph/s/m^2/sr can be obtained from the irradiance profile on the receiver in W/mm^2 by considering the size of the pinhole, the distance from the receiver, and the position at the receiver.

In this model, the detailed surface texture of the walls was not considered. Also, a plane wall was placed on the port with the same reflectance with the other walls. The influence of the surface texture on the global picture should be minor, as previously investigated by changing the surface reflectance property from specular to diffusive.[16] Concerning the reflection at the port, it is thought that the influence is likely to be less than 10% as considering the relative area of the port. The reflectance of the wall is changed from 0% to 70%. The reflectance would be ~10% for carbon wall case and 70% for tungsten wall case at the wavelength of 1000 nm.

IV. ERROR ASSESSMENT

A. Influence of reflection

Figure 9(a) shows the radiance, I_r, as a function of the major radius of the measurement positions. The reflectance, r, was changed from 0% to 70%. The radiance without reflection, I_0, is ~10^{15} ph/m^2/sr/s/Å at $R < 2.3$ m and had a peak at $R \sim 2.45$ m. The radiance in the LFS FOVs has approximately one order of magnitude greater than those of HFS FOVs. With increasing the reflectance, the radiance increases; when the reflectance was 70%, the profile of the radiance becomes almost flat at 2-3 × 10^{15} ph/m^2/sr/s/Å. In Fig. 9(b), the enhancement of radiance, which is defined as I_r/I_0, is shown for the cases of r = 10%, 30%, 50%, and 70%. The results indicate that the reflection increases the radiance by up to a factor of 20 in full W wall case in the low density discharge. Even in the case of carbon, the radiance can be increased by a factor of two at $R < 2.3$ m.

Figs. 9(c) and 9(d) show the profiles of the radiance and the enhancement of radiance, respectively, in the high density discharge. Similar to the low density discharge, the radiance increases with r from $R \sim 2.3$ m. In the high density discharge, the peak radiance does not change so much, but the reflection can increase the radiance in the region of $R \sim 2.3$ m by a factor of 1.5 (10%) to 10 (70%).

To assess measurement errors in LTS measurement, usually noise enhancement factor is introduced. In the core Thomson scattering cases, the enhancement factor should include the influence of the line emissions as well as the reflection. In the present case, however, it is likely that only the influence of the reflection is plausible, because the wavelength range is narrow and covers only in the near infrared wavelengths different from the core and edge Thomson scattering cases.[17]

Bremsstrahlung has a wavelength dependence and the dependence alters with changing the temperature. Without reflection, the photon radiance for a FOV can be obtained by line integrating the radiation along with the line of sight,

$$I(\lambda) = \int \frac{\epsilon_\lambda}{4\pi hc/\lambda} dl, \tag{2}$$

where h is the Planck constant, c is the speed of light, and 4π is used to obtain the power per unit solid angle. Since the variation in the wavelength dependence is not so significant in the measured temperature range, Eq. (2) can be simplified as

$$I(\lambda) \sim \frac{\overline{\epsilon_\lambda}}{4\pi hc/\lambda} l, \tag{3}$$

where $\overline{\epsilon_\lambda}$ is the averaged radiance along with the line of sight and l is the length of the radiation region in the FOV.

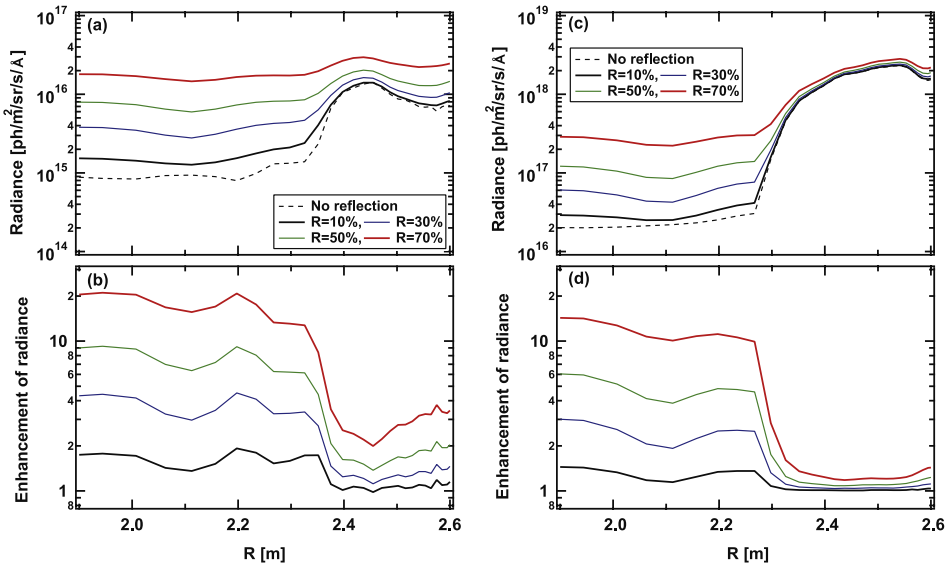

FIG. 9. (a) The radiance profile and (b) the enhancement of radiance as a function of the major radius of the measurement positions in the low density discharge. (c) and (d) show the radiance profile and the enhancement of radiance, respectively, in the high density scenario.

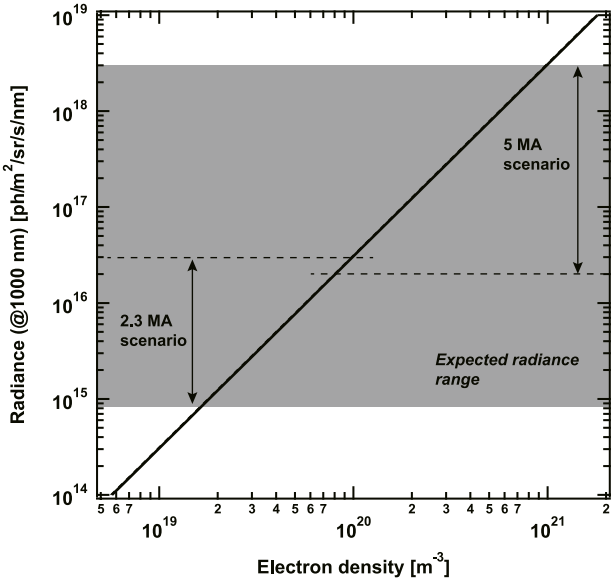

FIG. 10. The photon radiance calculated from Eq. (3) as a function of the density at 1000 nm assuming that $l = 1$ m.

Figure 10 shows the photon radiance calculated from Eq. (3) as a function of the density at 1000 nm assuming that $l = 1$ m. The weighted averaged T_e and Z_{eff} with the weight of the radiation of each cell were used in Eq. (3). In the low density case, the averaged T_e and Z_{eff} were 15.5 eV and 1.09, respectively, while they were 3.5 eV and 1.00, respectively, in the high density case. The averaged Z_{eff} should be greater without considering the weight of radiation; the averaged Z_{eff} becomes lower than that with considering the weight of radiation because the high density region has lower Z_{eff}. In Fig. 10, two lines are totally overlapped and did not see the difference at all. It can be said that the differences in T_e and Z_{eff} in the present ranges are negligible. From Figs. 9(a) and 9(c), it is seen that the radiance is from 1×10^{15} to 3×10^{16} ph/m^2/sr/s/Å in the low density discharge and from 2×10^{16} to 3×10^{18} ph/m^2/sr/s/Å in the high density discharge. Using the relation between the radiation and the density in Fig. 10, we can obtain the corresponding density; the corresponding density ranges are 1.5×10^{19}-10^{20} m^{-3} in the low density discharge and 8×10^{19}-10^{21} m^{-3} in the high density discharge. For the error assessment shown later, the radiance calculated using the averaged T_e and Z_{eff} and the corresponding density from Fig. 10 will be used as setting the enhancement factor to be unity.

TABLE III. Major parameters used in the numerical assessment.

Parameter	Value
Pulse width	10 ns
Laser diameter	7.5 or 10 mm
Laser pulse energy	3.5 or 7.0 J
Laser wavelength	1064 nm
Length of the scattering volume	30 or 60 mm
Effective path length of the plasma	1.0 m
Enhancement factor (K_e)	1
Excess noise factor (F_{noise})	2.5
Dark noise in a time slice (N_0)	30

B. Measurement error

Figures 11(a) and 11(b) show the errors in the density and temperature at the measurement point M in the low density discharge with three typical densities, 5×10^{18}, 1.5×10^{19}, and 5×10^{19} m^{-3}. In this calculation, the reflection of 10%, i.e., carbon wall case, was used to obtain the background radiance. The parameters used for the calculation were summarized in Table III. The laser pulse energy was assumed to be 3.5 J in Fig. 11. The errors decrease with increasing the density. It is seen from Fig. 6(a) that the actual density and temperature at the position M were 2×10^{19} m^{-3} and 100-150 eV, respectively; the errors in the density and temperatures are close to the case of the dotted lines in Figs. 11(a) and 11(b), respectively.

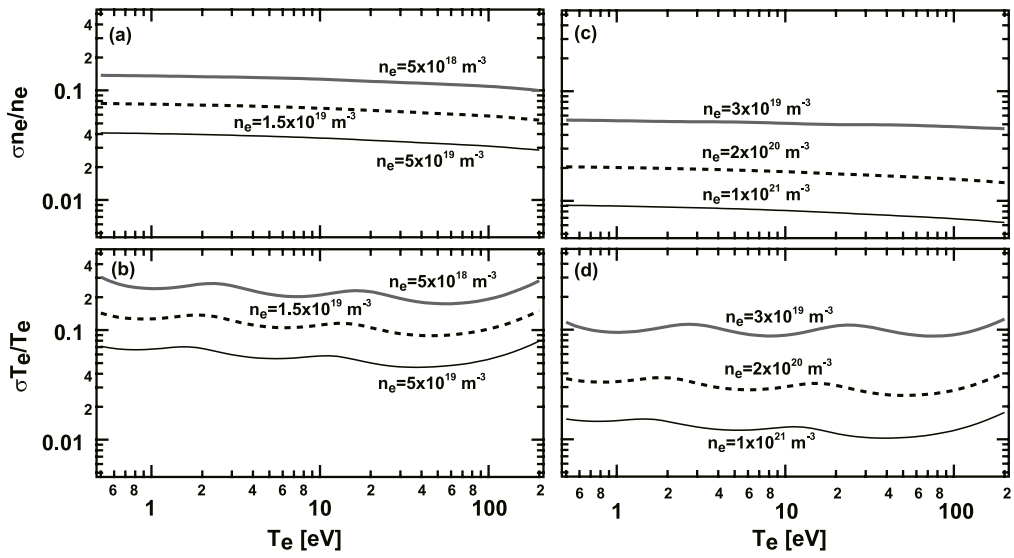

FIG. 11. The errors in (a) the density and (b) temperature at the measurement point M in the low density discharge with three different typical densities, 5×10^{18}, 1.5×10^{19}, and 5×10^{19} m^{-3}. (c) and (d) are the errors in the density and temperature, respectively, for high density discharge.

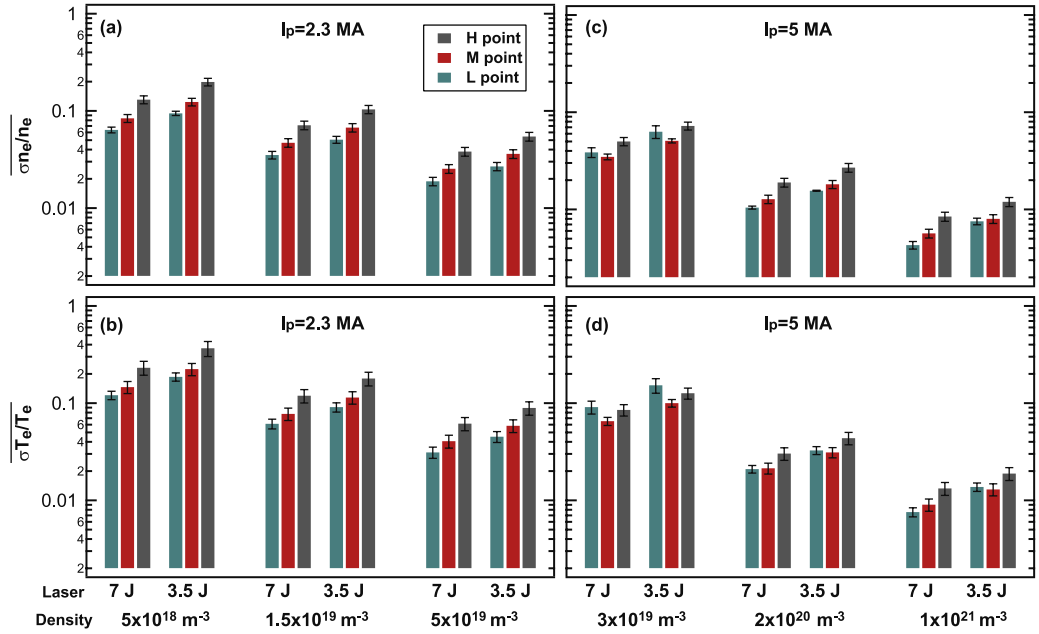

FIG. 12. Summary of the averaged errors in density and temperature in high density and low density discharges. Two different laser pulse energies, i.e., 3.5 and 7 J, were chosen.

Figures 11(c) and 11(d) show the errors in the density and temperature at the measurement point M in the high density discharge with three typical densities at the measurement position in the high density discharge, i.e., 3×10^{19}, 2×10^{20}, and 1×10^{21} m^{-3}. It is seen that the errors are less than those in the low density discharge, though the background radiance is much greater than that in the low density discharge.

In Fig. 12, the averaged errors in density and temperature in high density and low density discharges are summarized. Two different laser pulse energies were chosen. The 7 J case can decrease the measurement error by roughly 30%-40% from that in the 3.5 J case. The measurement error increases from L to H. Although the difference in the errors between L and M is not significant, the errors at H are much greater than those at M and L, because the solid angle is smaller. In the high density case, the error can be less than 20% even for H point, indicating that the parameters can be measured with reasonable errors. On the other hand, when the density is lower than 10^{19} m^{-3}, the measurement error is significantly high, say 40% in the temperature, with the laser pulse energy of 3.5 J.

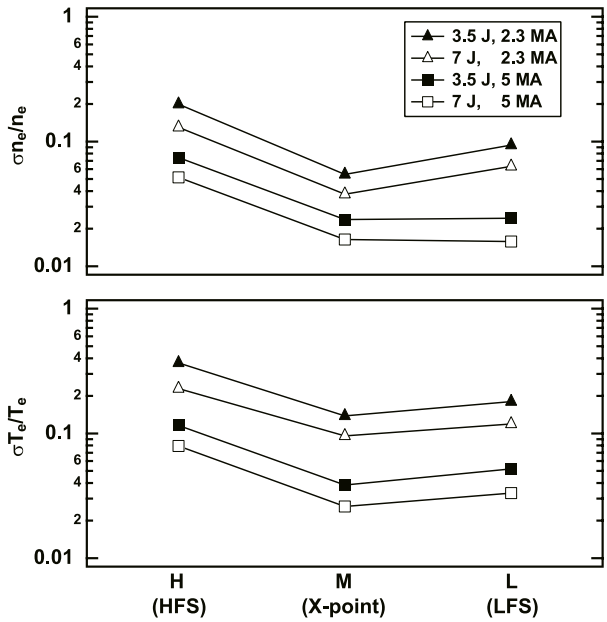

FIG. 13. The errors at H, M and L positions for high density and low density cases using the actual density and temperature at the measurement positions.

Considering the actual density and temperature at the measurement region shown in Fig. 5, the errors at the three positions are plotted for high density and low density cases in Fig. 13. In the high density discharge, the errors can be less than 10% in the temperature and density if we use 7 J laser pulse. It is likely that the measurement can be conducted with a reasonable accuracy. In the low density case, however, the errors at H would be fairly large, i.e., 40% in the temperature error and 20% in the density error even using 7 J laser pulse.

V. CONCLUSIONS

In this study, performance of the divertor Thomson scattering measurement system in the satellite tokamak JT-60SA was assessed in an accurate manner for an improved collection optical system. By offsetting the primary mirror position, the solid angle was increased as avoiding the interference of luminous flux by a factor of 2.3 times for low field side field of view and 5.6 times for high field side field of view. To assess the photon noise, bremsstrahlung radiation was calculated for typical two discharge cases, i.e., a low density case at I_p = 2.3 MA and a high density case at I_p = 5.5 MA. The plasma parameters were calculated by a SONIC code. In the low density discharge, the density in the measurement region was in the range of 5×10^{18}-5×10^{19} m^{-3}, while it would be

3×10^{19}-1×10^{21} m^{-3} in the high density discharge. The temperature was in the range of <170 eV.

To assess the influence of the light reflection at walls, ray trace simulations were conducted with the calculated bremsstrahlung radiation power profile and presently available computer aided design for JT-60SA using a commercially available ray tracing software LightTools. It was found that the radiation is stronger in the low field side compared with that in the high field side by more than an order of magnitude in both high and low density discharges. With increasing the wall reflection from 0% to 70%, the radiation increases especially in the high field side, where original radiation is low. When the reflectance was 10%, which corresponds to carbon wall case, the radiation would increase 1.5–2 times in the high field side. When the reflectance was 70%, which corresponds to tungsten wall case, the radiation increased 10-20 times in the high field side. Thus, compared with the carbon case, the measurement error can be increased in the full tungsten wall case by approximately three times at maximum.

The measurement errors in the density and temperature were assessed using the calculated radiation and target parameters. The wavelength ranges of the optical filter was optimized again for the present design, because the scattering angle was altered from the previous design. It was assessed that the errors in the density and temperature in the high density discharge can be 1.5%-5% from the X-point to low field side and 5%-10% at the high field side. It was found that the measurement can be properly conducted in the high density discharge including the high field side. On the other hand, in the low density case, the error could be increased by two to four times in the whole measurement region. The measurement performance in the high field side will be marginal. Based on the present design, we believe that we can proceed to the next step. Detailed design and engineering assessment should be conducted for mounting mechanism of optical elements, cooling capability, and alignment system etc.

ACKNOWLEDGMENTS

One of the authors thanks Dr. T. Nakano and Dr. E. Yatsuka from JAEA for useful discussion concerning the assessment of the radiation. This work was supported in part by JSPS KAKENHI Grant No. 15H04229.

[1]JT-60SA Research Plan: Research Objectives and Strategy, version 3.1, JT-60SA Research Unit, 2013.
[2]H. Kawashima, K. Hoshino, K. Shimizu, T. Takizuka, S. Ide, S. Sakurai, and N. Asakura, J. Nucl. Mater. **415**, S948 (2011).
[3]H. Tamai, N. Asakura, and N. Hosogane, J. Plasma Fusion Res. **74**, 1336 (1998), http://ci.nii.ac.jp/naid/110003826118/en/.
[4]T. N. Carlstrom, C. L. Hsieh, R. Stockdale, D. G. Nilson, and D. N. Hill, Rev. Sci. Instrum. **68**, 1195 (1997).
[5]N. Ohno, N. Tanaka, N. Ezumi, D. Nishijima, and S. Takamura, Contrib. Plasma Phys. **41**, 473 (2001).
[6]S. Kajita, N. Ohno, S. Takamura, and T. Nakano, Phys. Plasmas **13**, 013301 (2006).
[7]R. D. Monk, A. Loarte, A. Chankin, S. Clement, S. J. Davies, J. K. Ehrenberg, H. Y. Guo, J. Lingertat, G. F. Matthews, M. F. Stamp, and P. C. Stangeby, J. Nucl. Mater. **241-243**, 396 (1997).
[8]H. J. van der Meiden *et al.*, Rev. Sci. Instrum. **83**, 123505 (2012).
[9]F. Scotti and S. Kado, J. Nucl. Mater. **390-391**, 303 (2009).
[10]S. Kajita, T. Hatae, K. Itami, N. Ohno, and T. Nakano, J. Plasma Fusion Res. Ser. **9**, 157 (2010), http://www.jspf.or.jp/JPFRS/PDF/Vol9/jpfrs2010_09-157.pdf.
[11]S. Kajita, A. Enokuchi, T. Hatae, K. Itami, T. Hamano, S. Kado, N. Ohno, and N. Takeyama, Fusion Eng. Des. **89**, 69 (2014).
[12]K. Shimizu, T. Takizuka, K. Ohya, K. Inai, T. Nakano, A. Takayama, H. Kawashima, and K. Hoshino, Nucl. Fusion **49**, 065028 (2009).
[13]S. Kajita, R. Yasuhara, M. Sato, N. Ohno, M. Tokitani, and N. Yoshida, Opt. Express **21**, 17275 (2013).
[14]S. Kajita, T. Hatae, and O. Naito, Fusion Eng. Des. **84**, 2214 (2009).
[15]K. Kadota, M. Otsuka, and J. Fujita, Nucl. Fusion **20**, 209 (1980).
[16]S. Kajita, E. Veshchev, S. Lisgo, R. Barnsley, P. Morgan, M. Walsh, H. Ogawa, T. Sugie, and K. Itami, J. Nucl. Mater. **463**, 936 (2015).
[17]H. Tojo, T. Hatae, T. Sakuma, T. Hamano, K. Itami, Y. Aida, S. Suitoh, and D. Fujie, Rev. Sci. Instrum. **81**, 10D539 (2010).